Multi-axis force sensors: a state-of-the-art review

Jack O. Templeman[1], Brian B. Sheil[1] and Tong Sun[2]

[1]Department of Engineering Science, University of Oxford, Parks Road, Oxford OX1 3PJ, UK.

[2]City, University of London, Northampton Square, London EC1V 0HB, UK.

Main text wordcount: 4980

Figures: 19

Tables: 4

Initial submission, 20 May 2019

Revised submission, 10 November 2019

INTRODUCTION

Sensors capable of measuring multi-directional force, moment or combinations thereof are popular in a wide range of engineering research, including automation, machining processes, aerospace, medical applications and civil engineering. In this way, a single multi-axis sensor can perform what is essentially a three-dimensional (3D) measurement of physical quantities. These sensors are designed to produce an output signal in response to stimulation from a physical system of multiple force and moment components. In the vast majority of multi-axis force sensors this is achieved by using multiple strain-sensitive elements mounted on an elastic structure. The sensor structure is fundamental in determining important characteristics of the sensor such as stiffness, measurement range and isotropy, and any undesirable coupling between sensor outputs. Both the sensitive elements and the elastic structure require careful consideration to design a force sensor for accuracy, reliability and robustness.

The development of multi-axis force sensors has been considered extensively in the literature over the past seven decades. Furthermore, these sensors have been developed for widely varying requirements and conditions due to the broad range of potential applications. However, a collective resource which collates and examines this information does not exist. This paper presents a state-of-the-art review of multi-axis force sensing and sensor development. The basic concepts of force sensing and the adopted generalized framework are introduced. The fundamental strain sensing techniques adopted for the sensitive elements most commonly reported in the literature are also explored. Finally, a critical review of a large number of elastic structure designs is presented, broadly categorised as follows: (a) three degrees-of-freedom (DOF) cross-beam, (b) six DOF cross-beam, (c) column-type, (d) beam-column type and (e) Stewart platform.

SYSTEM DEFINITION

The system considered in this paper is defined in Figure 1. Convention defines the x and y axes in the plane of the sensor (lateral direction) and the z axis in the out-of-plane (vertical) direction. Therefore F_z and M_z denote axial force and moment respectively, F_x and F_y denote mutually orthogonal lateral forces and M_x and M_y denote mutually orthogonal lateral moments. The n force components may be assembled into a force vector $\boldsymbol{f}$ which, in the most general case, can be defined as:

$$\boldsymbol{f} = [F_x \quad F_y \quad F_z \quad M_x \quad M_y \quad M_z]^T \tag{1}$$

The respective outputs produced by the individual strain transducers within the sensor may be defined as an output vector $\boldsymbol{u}$ as follows:

$$\boldsymbol{u} = [u_1 \quad u_2 \quad u_3 \quad \dots \quad u_m]^T \tag{2}$$

where u_i denotes the output from the ith transducer and m is the total number of strain transducers. The relationship between the force and output vectors is therefore given by the matrix equation

$$\boldsymbol{u} = \boldsymbol{C}\boldsymbol{f} \tag{3}$$

where $\boldsymbol{C}$ is an $m \times n$ 'compliance matrix'. Although $\boldsymbol{C}$ can be determined analytically or numerically, it is most commonly determined experimentally through calibration tests (e.g. [1–3]). In a fully decoupled sensor, each output responds only to the application of a single corresponding load component. Coupling within a sensor, often referred to as 'crosstalk', means there are cross-sensitivities between the different channels such that the application of a particular load component influences multiple output signals.

STRAIN SENSING TECHNOLOGY

Electrical resistance strain gauging

Electrical resistance strain gauges (ERSGs) operate on the principle of an electrical conductor undergoing a change in electrical resistance due to geometry change. To obtain measurable output signals from the small resistance changes associated with ERSGs, they are commonly arranged in Wheatstone bridge circuits. This also facilitates temperature compensation where thermal-induced resistance changes apply to each arm of the bridge thereby mitigating any influence on the aggregated circuit output. A limitation of this sensing technology is vulnerability to electromagnetic (EM) interference and damage arising from water ingress into the sensor. ERSGs also have relatively low sensitivity, which can be a limitation in applications where a large sensor stiffness is required.

Fibre Bragg gratings

Although a number of optical strain measurement methods exist (e.g. Fabry-Perot interferometers, Rayleigh and Brillouin scattering), Fibre Bragg Gratings (FBGs) are the most popular for force measurement applications. FBGs are created by forming a periodic modulation of the refractive index along the core of a single-mode optical fibre. When a broadband spectrum of light is incident on an FBG within a fibre, a narrow band of the spectrum is reflected through coherent scattering at the grating index variations, as shown in Figure 2 [4,5]. The reflected spectrum is characterised by the Bragg wavelength, λ_B, which is defined as

$$\lambda_B = 2\, n_{eff}\, \Lambda \tag{4}$$

where n_{eff} is the mode effective refractive index and Λ is the grating period. If an FBG is mounted to a structure the change in wavelength, $\Delta\lambda_B$, can be related to strain, ϵ, or the change in temperature, ΔT, using the equation given in [6]:

$$\frac{\Delta\lambda_B}{\lambda_B} = (1 - P_e)\,\epsilon + \left(\alpha + \zeta + (1 - P_e)(\alpha_s - \alpha)\right)\Delta T \quad (5)$$

where α and α_s are the thermal expansion coefficients of the fibre and sensor structure respectively, and P_e and ζ are the photo-elastic and thermal-optic coefficients respectively of the fibre core.

Temperature compensation remains one of the major obstacles in the use of FBGs for force sensing. One of the most common methods is the use of a reference 'strain-free' FBG (e.g. [7]). However, a range of alternatives feature in the literature including dual-wavelength superimposed FBGs [8], dual-diameter FBGs [9,10] and the combination of an FBG with other structures, including long-period gratings [11], polarization-rocking filters [12] and superstructure FBGs [13]. Arguably one of the most effective methods is to perform arithmetic operations on two or more FBG measurements in a similar manner to that of a Wheatstone bridge (e.g. [14–16]). The use of FBGs as a strain sensing technology is desirable due to high sensitivity, immunity to EM interference and water damage and the ability to multiplex large numbers of FBGs along a single fibre. The comparatively high cost of FBG sensing compared to ERSGs, particularly with respect to optical interrogators, has slowed its adoption into broad industrial sectors however.

Semiconductor strain gauges

Semiconductor strain gauges (SSGs) are formed from a semiconducting material, most commonly silicon [17]. SSGs operate using the piezoresistive effect, which refers to the dependence of the electrical resistivity of a material on mechanical strain [18]. For a conductor subjected to a longitudinal strain ϵ, the gauge factor (GF) can be defined as

$$\mathrm{GF} = 1 + 2\nu + \left(\frac{1}{\epsilon}\,\frac{\Delta\rho}{\rho}\right) \quad (6)$$

where ν is the Poisson's ratio of the conductor material and ρ is the material resistivity which undergoes a change of $\Delta\rho$ [17–19]. The first two terms in Equation (6) correspond to the resistance

change due to changes in the conductor geometry, while the last term corresponds to change in the conductor material resistivity [18,19]. SSGs typically have a significantly greater strain sensitivity than metallic strain gauges, due to the greater change in resistivity under strain [20]. However, one of the most important applications of SSGs is in Micro-electro-mechanical systems (MEMS) force sensors, as micro-machining techniques allow them to be constructed at a much smaller scale.

Capacitive sensing

A capacitor is a component comprising electrical conductors separated by a non-conductive layer formed from a dielectric medium. When a potential difference is applied to the capacitor, an electric field is induced across the dielectric layer. This produces a net positive electrical charge developing on one conductor and a net negative charge on the other. For a simple capacitor consisting of two parallel plates of cross-sectional area A, separated by a uniform gap of thickness d, the capacitance, C, is given by

$$C = \frac{\epsilon_0 \, \epsilon_r \, A}{d} \tag{7}$$

where ϵ_0 and ϵ_r are the permittivity of free space and dielectric material forming the gap respectively and $d \ll A$. Capacitive sensing can achieve high sensitivity, allowing measurement of very small deflections [21]. Similar to SSGs, capacitors can be created through micro-machining techniques, facilitating very small-scale force measurement. Capacitive sensing also allows the creation of flexible sensors, which has led to their adoption in measuring tactile information [22].

THREE DOF CROSS-BEAM SENSORS

One of the most widely adopted multi-axis force sensor designs is the ‘cross-beam’ or ‘Maltese cross’ type. This design typically consists of an outer frame connected to a central platform by three or more elastic beam members. The most common arrangement comprises four beams arranged in a planar

cross-shape, as illustrated in Figure 3. In this case, application of an in-plane force, such as F_x and / or F_y, induces axial deformation in the members parallel to the load, as well as lateral bending in the members perpendicular to the load. Application of an axial force F_z and moment M_z induce out-of-plane bending and lateral bending respectively in all four members. Lateral moments M_x and / or M_y induce vertical bending and torsion in the members perpendicular and parallel to the moment axis respectively. Collinearity between the *x* and *y* loading directions and the elastic beams in a four-spoke beam design assists decoupling of sensor outputs and maximises the strain in the beams, whilst also achieving an identical response for mutually orthogonal lateral forces and moments. Table 1 presents a comprehensive list of three DOF force sensors documented in the literature. Only the salient studies are discussed in further detail below. The three DOF load combinations that have been considered in the literature are as follows:

(a) F_x, F_y, F_z (3DOF-A): the upper and lower surfaces of the elastic beams are instrumented, which are typically designed with low vertical bending resistance. F_x and F_y are generally applied at a vertical offset to the cross centre, such that they induce out-of-plane bending.

(b) F_x, F_y, M_z (3DOF-B): the lateral surfaces of the elastic beams are instrumented, which are typically designed with low lateral bending resistance.

(c) F_z, M_x, M_y (3DOF-C): similar to 3DOF-A.

Valdastri et al. [23] presented a piezoresistive 'micro' 3DOF-A cross-beam design. The force components are applied to the sensor at a fixed vertical offset via a rigid rod attached to the central platform. Measurement of the out of-plane deformations of the cross-beams was used to resolve the applied lateral forces. The cross-beam structure is etched from silicon wafer with one p-type silicon piezoresistor per beam, obtained via ion implantation, arranged in four quarter Wheatstone bridge circuits. Fontana et al. [24] described a larger scale 3DOF-A cross-beam design operating on similar principles, except using four Wheatstone bridges comprising 16 ERSGs. Bekhti et al. [25]

documented a miniature 3DOF-A design employing capacitive sensing. A plastic cross-beam was mounted on a conductive plate and supported above a printed circuit board (PCB), forming four capacitors in a square grid. Each of the four beam members was formed from two compliant laterally-spaced beams as shown in Figure 4. Xiong et al. [26] proposed a 3DOF-A cross-beam sensor for robot plantar force measurement, using a total of five FBGs for strain sensing (see Figure 5). Decoupling of measurements and temperature compensation were achieved by forming each sensor output as the difference between two FBG wavelength shifts.

Kim et al. [27] presented a 3DOF-B sensor in which the beams were laterally-compliant. The novelty of this design is centred around the use of additional compliant beams in the outer frame, to promote decoupling of sensor output (see Figure 6). The compliant elements were instrumented with a total of 40 ERSGs. Fernandez Fernandez et al. [14] documented a 3DOF-C sensor applied to the control of robots in 'EM noisy environments'. Those authors adopted a classic rigid four-beam structure, resembling that shown in Figure 3, instrumented with eight FBGs. The sensor outputs were created by taking the difference between the wavelength shifts of the FBGs on opposite sides of each beam; this had the added advantage of achieving temperature compensation.

SIX DOF CROSS-BEAM SENSORS

Rigid jointed cross-beams

Six DOF cross-beam force sensors typically require strain-sensing elements on all sides of the elastic members [28]. To achieve similar lateral and vertical compliance, square beam cross-sections are common [24]. In its most rudimentary form, a six DOF cross-beam comprises rigid frame-beam and platform-beam joints. Table 2 provides a broad list of six DOF cross-beam sensors documented in the literature. Chao and Yin [3] adopted a design similar to that presented in Figure 3 to measure the reaction load on a human foot during locomotion. However, the use of rigid joints was shown to

148 reduce measurement isotropy and measurements also showed a high degree of coupling [29,30]. Kim
149 et al. [31] presented a cross-type design in which grooves were machined into the beams to
150 incorporate capacitive sensing, as shown in Figure 7. Each groove was filled with dielectric elastomer
151 positioned between two conductive electrodes. Application of a load to the central platform causes a
152 contraction of the grooves thereby altering the capacitance of the sensing elements. Palli et al. [32]
153 proposed a cross-beam design coupled with optoelectronic sensing. In this design, deflection of the
154 cross-beam is measured by changes in the light received by a series of photodetectors from light
155 emitting diodes through relative movement of a reflective surface. Although less common, Lin et al.
156 [33] and Feng et al. [34] proposed 'double-cross' designs using eight elastic beam elements for wheel
157 force measurement (see Figure 8). The redundant spokes provided additional structural capacity. The
158 3DOF-B design proposed by [33] was extended in [34] to 6DOF measurement by placing additional
159 strain-sensitive elements on the top and bottom surfaces of the eight beams.

160 *Flexible jointed cross-beams*

161 The use of flexible elements in the outer frame has featured frequently in the literature to minimise
162 coupling between sensor outputs. Flexible frame-beam joints are analogous to sliding universal joints
163 when compliance in three DOF is introduced, namely displacement parallel to the beam axis and
164 rotation about two mutually orthogonal axes, both of which are perpendicular to the beam axis [28].
165 This allows the sensor body to be manufactured monolithically but does not introduce any undesirable
166 behaviours associated with mechanical connections, such as friction and clearances.

167 Scheinman [35] documented one of the earliest designs of this type for use in wrist force sensing,
168 described later in detail in [36]. This cross-beam design features thin flexures machined into the outer
169 frame at the frame-beam joints. The four cross-beam members were instrumented with 16 SSGs (one
170 placed on all surfaces of each beam). A similar design was presented by Van Brussel et al. [37] using
171 ERSGs, as shown in Figure 9. The flexures were dimensioned to simulate ball-hinge behaviour. Chao

and Chen [38] modified the traditional cross-beam design to include ball-bearings at the frame-beam joints (see Figure 10). The design was shown to have high sensitivity and significantly improved measurement isotropy compared to an equivalent fixed-joint design. Dao et al. [39] documented a micro cross-beam sensor using piezoresistive strain-sensing for measuring the fluctuating force and moment components on a particle at the bed of a turbulent channel flow. The cross-beam was fabricated on a micro sensing chip from n-type silicon using a micromachining process. Eighteen piezoresistors formed using impurity diffusion were located on the upper surface of the beams. Shi and Hall [40] presented a cross-beam wheel force sensor using radial spherical plain bearings at the frame-beam joints. Compared with the design in [38], this design freed the three rotational DOF and the radial displacement at the frame-beam joints. Ma and Song [41] developed a simplified analytical model of a cross-beam with compliant frame elements using Timoshenko beam theory, to explore the strain distributions along the elastic beams.

The design documented by Kim [42] uses ‘parallel-plate beams’ in the outer frame to achieve lower deflection and rotation due to bending moment and axial moment respectively. Kim et al. [43] documented an extension of this design in which the beam members are also modified. Each beam contained both a vertically and laterally compliant parallel-plate-beam. Both versions of this sensor required 24 ERSGs. A significantly more complex structure was documented by Mastinu et al. [44] and Gobbi et al. [45] involving a three-spoked design with 'sliding spherical joints' at the frame-beam joints. The joints are designed to allow four DOF: three rotations and displacement parallel to the beam axis. Mastinu et al. [44] documented the design development of this sensor whereas Gobbi et al. [45] presented the sensor construction and experimental assessment. The design demonstrated good linearity and a maximum coupling error of < 1%. Sun et al. [46] presented another force sensor in which the outer frame contained highly-compliant plates (see Figure 11). To increase sensitivity, each cross-member contains a single vertically-orientated blind hole and is instrumented to measure 3DOF-B loads. Similarly, the frame contains horizontally-orientated through-holes and are

197 instrumented for measurement of 3DOF-C loads. The frame also contains thin, laterally compliant
198 plates to connect the structure to the fixed corner points. Interestingly, the layout of the ERSGs on
199 the cross-beams differ to that typically adopted in the literature in that they are orientated in the shear
200 direction i.e. at 45° to the beam axis.

201 Kang et al. [30] undertook an optimization exercise using finite element analysis to minimise coupling
202 error in a six DOF cross-beam sensor. For the purpose of this review, the deformed shape of this
203 sensor subjected to F_z, F_y, M_z and M_x loading was explored using a Solidworks 2019 (perfectly-
204 elastic) finite element analysis (FEA). The results are presented in Figure 12 where contours indicate
205 the magnitude of the resultant displacements. Although these results are only indicative, it can be
206 seen that significant deformations occur at the flexible joints. It was demonstrated in [30] that this
207 flexible joint behaviour achieved a coupling error of < 3.2%, determined using both numerical
208 analysis and experimental testing. Kazerooni and Akbari [47] progressed this work by proposing a
209 modified optimization formulation to reduce the coupling error to < 1.5%. Similar designs include
210 the sensor documented by Schickl et al. [48] for use in measurement of forces in the feet of humanoid
211 robots and the large sensor documented by Chen et al. [49] for robotic manipulator control in space
212 applications. Huang et al. [50] presented analysis of a very similar sensor structure to in [30], except
213 instrumented with a total of 16 FBGs, with one placed on each side of the four cross beams. Similar
214 to the design in [14], the sensor outputs were formed from the wavelength shift difference between
215 FBGs on opposite sides of each beam, which also achieves temperature compensation. The 8 × 6
216 compliance matrix for this design was determined using both 3D FEA and an analytical Timoshenko
217 beam theory model developed in [51].

218 *Dual-layer cross-beams*

219 These sensors involve a vertical assembly of two cross-beam sensors, where each cross-beam is
220 tasked with the measurement of a specific three DOF load combination. The design documented by

Kim et al. [52] combined the 3DOF-B load cell reported in Kim et al. [27] (shown in Figure 6) with a lower 3DOF-C cross-beam. The two cross-beams are connected through the outer frames and were instrumented with ERSGs. In the dual sensor proposed by Yuan et al. [53], an upper 3DOF-B and a lower 3DOF-C cross-beam are connected via the central platforms. Rigid frame-beam joints with vertically compliant beams were adopted for the upper cross-beam with a total of eight ERSGs on the upper and lower surfaces of the beams. The lower cross beam comprised flexible frame-beam joints and laterally-compliant beam elements featuring a total of eight ERSGs mounted on the beam side surfaces. Wu and Cai [54] proposed a dual-layer cross-beam involving an upper 3DOF-B and a lower 3DOF-C. The beam ends were located within grooves in an outer cylindrical shell as shown in Figure 13. Each beam contains a 'double-hole' to create a double bending-beam. Although the sliding frame-beam joints were intended to decouple sensor outputs, those authors noted that very accurate sliding clearances were required to achieve this.

COLUMN-TYPE SENSORS

Column-type sensors typically feature an elastic body made of a single prismatic element which is fixed at one end and free to deflect and rotate at the other. Loads applied to the sensor at the free end induce a strain field in the elastic body which is measured by various combinations of strain-sensitive elements. The most commonly-adopted column-type load cell design features a cylindrical elastic body, such as that shown in Figure 14. Typically only the outside surface is instrumented, as it experiences the greatest strains and mounting the strain sensing elements is more straightforward. Table 3 provides a summary of column-type sensors that have featured in the literature. The main advantages of the column-type are its simplicity and robustness. Column-type sensors also exhibit significantly greater stiffness in the vertical direction compared to cross-beam sensors [55]. The main disadvantage associated with these sensors is poor measurement isotropy and low sensitivity to F_z. In particular, there are unavoidable couplings between the measurements of lateral forces and lateral

moments. The column also needs to be sufficiently long to ensure strain sensing elements are not located within the non-uniform strain distributions towards the ends.

The earliest column-type designs referenced in the literature are related to biomechanics applications. Cunningham and Brown [56] presented a method for the measurement of human gait involving a rectangular plate supported by four column-type load cells at the corners. The columns were tubular cylinders, machined from a solid bar, with ERSGs mounted on the outside surface. End flanges enabled bolted connections to the plate and base. Paul [57] reported similar force plate designs to that in [56] except each column was instrumented with twelve silicon SSGs rather than ERSGs. The SSGs were arranged in three layers along the length of the column and formed six bridge circuit outputs for the six load components acting on the force plate. Berme et al. [1] presented a reduced-length design to facilitate inclusion within the pylon of a prosthesis. Instead of deriving the lateral forces using the difference in bending moment at two axial positions, the shear forces were measured directly using strain gauges orientated ± 45° to the cylinder axis. Van Brussel et al. [37] presented a six-axis design consisting of two rigid rings connected by four vertical flexural strips. The design resembles a cylindrical column with four large sections at the cardinal points of the wall removed. 3DOF-B loads are related to the shear strain in the flexural strips, whereas 3DOF-C loads are obtained from the bending and compression strains. Byrne and Houlsby [2] used a column-type load cell design for the measurement of six DOF loading applied to a model foundation on sand (see Figure 14). A total of 32 ERSGs were bonded to the outer surface of the cylinder in groups of four and positioned at eight circumferential locations. This provided six full Wheatstone bridge circuits corresponding to each of the six DOF load components. Van der Laag [15] extended this work to develop a sensor employing a combination of both ERSGs and FBGs. 32 ERSGs were mounted on the outside surface to form eight full Wheatstone bridges whereas 32 and 14 FBGs were located on the outer and inner surfaces respectively. Arithmetic operations performed on the outputs of two or more FBGs, in a similar manner to Wheatstone bridge circuits, were used to achieve load and temperature isolation. That

author noted that while both the ERSGs and FBGs provided accurate results, difficulties in mounting FBGs to the sensor structure were identified.

BEAM-COLUMN SENSORS

Although much less common, beam-column force sensors generally consist of both elastic beam and column elements that undergo deformation during loading. Stroud [58] documented one of the more popular designs of this type which was later described in greater detail by Bransby [59] (see Figure 15). The design features four vertical columns and four horizontal beams which connect an upper and lower 'block'. The columns and beams are designed to be flexible in bending. F_z induces axial compression in the vertical columns whereas F_x induces tension in one pair of horizontal beams and compression in the other pair [59]. ERSGs are mounted on both faces of all eight elastic elements to form three Wheatstone bridge circuits. Huang et al. [60] proposed a robot wrist force sensor using a cross-beam supported by four vertical beams connected to an outer frame, as shown in Figure 16. Lateral forces and axial moment are measured by bending deformation of the vertical beams using ERSGs. The lateral moments and axial force are measured through conventional out-of-plane bending of the cross members.

STEWART PLATFORM SENSORS

Stewart [61] originally described the Stewart platform as a six DOF mechanism, consisting of a rigid plate (referred to as the platform) which is connected to a fixed base by six legs, as shown in Figure 17. The legs are formed from elastic members which can be instrumented to measure load-induced axial deformations. Stewart platform sensors generally have the characteristics of high stiffness and load capacity, through distributing the loading axially over the six legs. To achieve a six DOF mechanism, at least one spherical joint is required on each leg whereas the other joint can be either a universal or spherical joint [62]. To convert the Stewart platform into a force sensor, the same joint

configuration is required to ensure that the deformations in the legs are purely axial. A summary of Stewart platform force sensors documented in the literature is given in Table 4.

Romiti and Sorli [63] presented an early six DOF Stewart platform force sensor using six single-axis force sensors as platform legs. The legs were connected to the two platforms via low-friction ball joints. Sorli and Zhmuď [64] and Ferraresi et al. [65] subsequently developed a prototype of this design where experimental investigations revealed a very high stiffness to the applied loads. However, hysteresis and non-linearity was observed in the sensor output due to backlash in the ball joints [64]. Dai and Kerr [66] proposed using six pre-tensioned flexible wire legs to ensure transferral of axial forces only. The force in each wire was measured using six elastic cantilevers fixed to the sensor base, instrumented with ERSGs. Kang [62] proposed platform legs comprising two springs located at either end of a 'core'. A linear variable differential transformer (LVDT) was mounted on each leg to measure axial deflections under the applied loads. The legs were connected to the base and platform using ball and socket joints. Dwarakanath et al. [67] documented a Stewart platform design employing bending rings in the sensor legs (see Figure 18). The rings introduced compliance into the system and facilitated concentration of strain. However, some inaccuracies and repeatability issues were encountered arising from clearances in the ball and socket joints used to connect the legs to the platform and base.

Zhenlin et al. [68] presented a parallel mechanism force sensor described as a variant on the Stewart platform. Six elastic legs, arranged in three pairs, were used to connect three orthogonal sides of a cube-shaped platform to the base. A monolithic structure was possible by adopting flexural hinges instead of the traditional spherical joints. This structure showed improved measurement isotropy over the traditional Stewart platform structure geometry. Ranganath et al. [69] and Bhavikatti et al. [70] proposed using Stewart platform-type geometries in 'near singular' configurations. This amplified the forces experienced by the legs thereby creating a highly sensitive force sensor for specific load

components. The prototypes developed in [69,70] had heightened sensitivity to 3DOF-B loads and the three moments respectively. Both designs employed flexural hinges for the leg joints and ring structures instrumented with ERSGs on each leg. Seibold et al. [71] presented a small-scale sensor as part of an articulated grasping instrument for minimally invasive robotic surgery applications. This design used ERSGs and flexural joints and was sufficiently small to fit within a 10 mm diameter sphere. Luo et al. [72] presented another small-scale design for use in robotic fingers. The sensor legs were created from small brazen pipes ending in ball joints, created from rod end bearing and knuckle joints. By having two legs meet at each ball joint, only six joints are required in this design. Yao et al. [73] proposed the use of a pre-stress to improve the performance of mechanical spherical joints within the structure. An adjustable seventh leg spanning between the platform and base along the sensor centreline was used to induce a compressive force in the six platform legs. This prevented the development of tension in the legs towards mitigating errors arising from non-linearity and mechanical hysteresis in the joints.

Dwarakanath and Venkatesh [74] presented an alternative 'joint-less' design to overcome the limitations of conventional mechanical and flexural joints. The design involved legs with conical ends which rest in a spherical indentation on both the platform and base. The legs were secured in place by a compressive pre-load using deadweight. Figure 19 shows the design proposed by Müller et al. [75] using free-spanning, pre-tensioned FBGs as structures legs. This approach relies on having a separate central cylinder structure to support the platform. The fibre was glued at support locations on the base and platform after pre-tensioning and strain is induced in the FBGs by the relative change in distance between these fixation points. A similar design was also presented by Kim and Lee [76]. The sensors described in [75,76] did not consider temperature compensation despite the experimental results in [76] confirming the sensor outputs to be temperature dependent. Another FBG-based design was proposed by Haslinger et al. [77], in which each leg is formed from a steel capillary with an optical fibre containing an FBG bonded into the centre. The legs are bonded to top and bottom plates

342 with structural epoxy, forming a relatively rigid joint. The effect of any bending of the legs is limited
343 by the FBGs being mounted within the centre of the capillaries and therefore on the neutral axis.
344 Temperature compensation is achieved in this design using an additional strain free FBG, mounted
345 in a steel capillary bonded to the baseplate.

346 **DISCUSSION AND CONCLUSIONS**

347 This paper has described a comprehensive review of multi-axis force sensors documented in the
348 literature over the past seven decades. The review first considered strain sensing technology used in
349 multi-axis force sensors. Electrical resistance strain gauges have for decades been the standard
350 mechanism for measuring strain induced on the sensor structure. Despite their ubiquity, these sensors
351 have inherent limitations that make their usage challenging, or indeed impractical, in many
352 applications. Specifically, the advantages fibre Bragg gratings offer include: (a) immunity to
353 electromagnetic interference, (b) reduced size and weight, (c) superior strain resolution, (d)
354 environmental ruggedness and (e) optical multiplexing. Although semiconductor strain gauges and
355 capacitive sensing have featured in the literature, they are primarily used in exceptional circumstances
356 such as in miniature force sensors.

357 The review of the elastic host structures highlighted the large variability of designs that have been
358 developed, perhaps understandably given the wide range of applications covered by this review.
359 Designs were broadly grouped as: (a) three DOF cross-beams, (b) six DOF cross-beams, (c) column-
360 type sensor, (d) column-beam sensors and (e) Stewart platform sensors. Cross-beam sensors appear
361 to have had much success as multi-axis force sensors in a range of configurations and applications.
362 Designs employing flexible-joints and features to concentrate strain have been shown to improve the
363 sensitivity and minimise coupling error of the sensor outputs. The main disadvantage associated with
364 these sensors is the considerable flexibility in the vertical direction as deformations are primarily in
365 bending. Column-type sensors are desirable due to their simple structure (and low fabrication costs),

and the high stiffness in the vertical direction. However, accurate measurement of the applied forces requires sensing of a complex strain field induced on the sensor host structure. To achieve a high degree of accuracy, sensing elements are required to be placed at exact locations and orientations. Although Stewart platforms have been shown to be effective, the literature has highlighted many issues associated with the development of the complex structure in conjunction with flexible joints.

Based on this review, there appears to be a concerted effort to develop force sensors employing FBG strain sensing. While the use of fibre optics in force sensors offers opportunities to re-visit simplified host structures, temperature compensation remains one of the major obstacles. The relatively high cost of optical analysers has also slowed its adoption into broad industrial sectors. Rapid advancements in 3D printing also present exciting opportunities for the development of more rigorous, complex host structures that were once considered either impractical or undesirable (due to fabrication costs).

ACKNOWLEDGEMENT

This project was supported by the Royal Academy of Engineering under the Research Fellowship Scheme.

REFERENCES

[1] N. Berme, P. Lawes, S. Solomonidis, J.P. Paul, A Shorter Pylon Transducer for Measurement of Prosthetic Forces and Moments during Amputee Gait, Eng. Med. 4 (1975) 6–8. https://doi.org/10.1243/EMED_JOUR_1975_004_032_02.

[2] B.W. Byrne, G.T. Houlsby, Investigating 6 degree-of-freedom loading on shallow foundations, in: Proceedings of the First International Symposium of Frontiers in Offshore Geotechnics, CRC Press, Perth, Australia, 2005: pp. 477–482. https://doi.org/10.1201/NOE0415390637.

[3] L.-P. Chao, C.-Y. Yin, The six-component force sensor for measuring the loading of the feet in locomotion, Mater. Des. 20 (1999) 237–244. https://doi.org/10.1016/S0261-3069(99)00009-6.

[4] K.O. Hill, G. Meltz, Fiber Bragg grating technology fundamentals and overview, J. Lightwave Technol. 15 (1997) 1263–1276. https://doi.org/10.1049/el:19910971.

[5] A. Othonos, Fiber Bragg gratings, Rev. Sci. Instrum. 68 (1997) 4309–4341. https://doi.org/10.1063/1.1148392.

[6] S. Magne, S. Rougeault, M. Vilela, P. Ferdinand, State-of-strain evaluation with fiber Bragg grating rosettes: application to discrimination between strain and temperature effects in fiber sensors, Appl. Opt. 36 (1997) 9437–9447. https://doi.org/10.1364/AO.36.009437.

[7] A.D. Kersey, T.A. Berkoff, W.W. Morey, Fiber-optic Bragg grating strain sensor with drift-compensated high-resolution interferometric wavelength-shift detection, Opt. Lett. 18 (1993) 72–74. https://doi.org/10.1364/OL.18.000072.

[8] M.G. Xu, J.-L. Archambault, L. Reekie, J.P. Dakin, Discrimination between strain and temperature effects using dual-wavelength fibre grating sensors, Electron. Lett. 30 (1994) 1085–1087. https://doi.org/10.1049/el:19940746.

[9] S.W. James, M.L. Dockney, R.P. Tatam, Simultaneous independent temperature and strain measurement using in-fibre Bragg grating sensors, Electron. Lett. 32 (1996) 1133–1134. https://doi.org/10.1049/el:19960732.

[10] M. Song, S.B. Lee, S.S. Choi, B. Lee, Interferometric temperature-insensitive strain measurement with use of different-diameter fiber Bragg gratings, in: CLEO '97 - Summaries of Papers Presented at the Conference on Lasers and Electro-Optics, IEEE, Baltimore, Maryland, USA, 1997: p. 419. https://doi.org/10.1109/CLEO.1997.603358.

411 [11] H.J. Patrick, G.M. Williams, A.D. Kersey, J.R. Pedrazzani, A.M. Vengsarkar, Hybrid Fiber
412 Bragg Grating/Long Period Fiber Grating Sensor for Strain/Temperature Discrimination, IEEE
413 Photon. Technol. Lett. 8 (1996) 1223–1225. https://doi.org/10.1109/68.531843.

414 [12] S.E. Kanellopoulos, V.A. Handerek, A.J. Rogers, Simultaneous strain and temperature
415 sensing with photogenerated in-fiber gratings, Opt. Lett. 20 (1995) 333–335.
416 https://doi.org/10.1364/OL.20.000333.

417 [13] B.-O. Guan, H.-Y. Tam, X.-M. Tao, X.-Y. Dong, Simultaneous strain and temperature
418 measurement using a superstructure fiber Bragg grating, IEEE Photon. Technol. Lett. 12 (2000) 675–
419 677. https://doi.org/10.1109/68.849081.

420 [14] A. Fernandez Fernandez, F. Berghmans, B. Brichard, P. Mégret, M. Decréton, M. Blondel,
421 A. Delchambre, Multi-component force sensor based on multiplexed fibre Bragg grating strain
422 sensors, Meas. Sci. Technol. 12 (2001) 810–813. https://doi.org/10.1088/0957-0233/12/7/310.

423 [15] D.A.M. van der Laag, Design and Calibration of a Multi-Axial Load Cell for Quasi-Static and
424 Dynamic Testing, MSc Thesis, Delft University of Technology, 2016.

425 [16] M.G. Xu, J.-L. Archambault, L. Reekie, J.P. Dakin, Thermally-compensated bending gauge
426 using surface-mounted fibre gratings, Int. J. Optoelectron. 9 (1994) 281–283.

427 [17] H.-P. Phan, D.V. Dao, K. Nakamura, S. Dimitrijev, N.-T. Nguyen, The Piezoresistive Effect
428 of SiC for MEMS Sensors at High Temperatures: A Review, J. Microelectromech. Syst. 24 (2015)
429 1663–1677. https://doi.org/10.1109/JMEMS.2015.2470132.

430 [18] E.O. Doebelin, Measurement Systems: Application and Design, 4th ed., McGraw-Hill, New
431 York, 1990.

432 [19] Y. Kanda, Piezoresistance effect of silicon, Sens. Actuator A Phys. 28 (1991) 83–91.
433 https://doi.org/10.1016/0924-4247(91)85017-I.

[20] W.P. Mason, R.N. Thurston, Use of Piezoresistive Materials in the Measurement of Displacement, Force, and Torque, J. Acoust. Soc. Am. 29 (1957) 1096–1101. https://doi.org/10.1121/1.1908710.

[21] P. Puangmali, K. Althoefer, L.D. Seneviratne, D. Murphy, P. Dasgupta, State-of-the-Art in Force and Tactile Sensing for Minimally Invasive Surgery, IEEE Sens. J. 8 (2008) 371–381. https://doi.org/10.1109/JSEN.2008.917481.

[22] A.L. Trejos, R.V. Patel, M.D. Naish, Force sensing and its application in minimally invasive surgery and therapy: a survey, Proc. Inst. Mech. Eng. C. 224 (2010) 1435–1454. https://doi.org/10.1243/09544062JMES1917.

[23] P. Valdastri, S. Roccella, L. Beccai, E. Cattin, A. Menciassi, M.C. Carrozza, P. Dario, Characterization of a novel hybrid silicon three-axial force sensor, Sens. Actuator A Phys. 123–124 (2005) 249–257. https://doi.org/10.1016/j.sna.2005.01.006.

[24] M. Fontana, S. Marcheschi, F. Salsedo, M. Bergamasco, A Three-Axis Force Sensor for Dual Finger Haptic Interfaces, Sensors. 12 (2012) 13598–13616. https://doi.org/10.3390/s121013598.

[25] R. Bekhti, V. Duchaine, P. Cardou, Miniature capacitive three-axis force sensor, in: 2014 IEEE/RSJ International Conference on Intelligent Robots and Systems, IEEE, Chicago, Illinois, USA, 2014: pp. 3939–3946. https://doi.org/10.1109/IROS.2014.6943116.

[26] L. Xiong, G. Jiang, Y. Guo, H. Liu, A Three-Dimensional Fiber Bragg Grating Force Sensor for Robot, IEEE Sens. J. 18 (2018) 3632–3639. https://doi.org/10.1109/JSEN.2018.2812820.

[27] G.-S. Kim, D.-I. Kang, S.-H. Rhee, K.-W. Um, Design and fabrication of a three-component force/moment sensor using plate-beams, Meas. Sci. Technol. 10 (1999) 295–301. https://doi.org/10.1088/0957-0233/10/4/005.

[28] D.M. Gorinevsky, A.M. Formalsky, A.Y. Schneider, Force Control of Robotic Systems, 4th ed., CRC Press, Boca Raton, 1997.

[29] S.A. Liu, H.L. Tzo, A novel six-component force sensor of good measurement isotropy and sensitivities, Sens. Actuator A Phys. 100 (2002) 223–230. https://doi.org/10.1016/S0924-4247(02)00135-8.

[30] M.-K. Kang, S. Lee, J.-H. Kim, Shape optimization of a mechanically decoupled six-axis force/torque sensor, Sens. Actuator A Phys. 209 (2014) 41–51. https://doi.org/10.1016/j.sna.2014.01.001.

[31] D. Kim, C.H. Lee, B.C. Kim, D.H. Lee, H.S. Lee, C.T. Nguyen, U.K. Kim, T.D. Nguyen, H. Moon, J.C. Koo, J.-D. Nam, H.R. Choi, Six-axis capacitive force/torque sensor based on dielectric elastomer, in: Proceedings of SPIE 8687, Electroactive Polymer Actuators and Devices (EAPAD) 2013, SPIE, San Diego, California, USA, 2013: pp. 1–9. https://doi.org/10.1117/12.2009970.

[32] G. Palli, L. Moriello, U. Scarcia, C. Melchiorri, Development of an optoelectronic 6-axis force/torque sensor for robotic applications, Sens. Actuator A Phys. 220 (2014) 333–346. https://doi.org/10.1016/j.sna.2014.09.023.

[33] G. Lin, H. Pang, W. Zhang, D. Wang, L. Feng, A self-decoupled three-axis force sensor for measuring the wheel force, Proc. Inst. Mech. Eng. D. 228 (2014) 319–334. https://doi.org/10.1177/0954407013508278.

[34] L. Feng, G. Lin, Z. W, H. Pang, T. Wang, Design and optimization of a self-decoupled six-axis wheel force transducer for a heavy truck, Proc. Inst. Mech. Eng. D. 229 (2015) 1585–1610. https://doi.org/10.1177/0954407014566439.

[35] V.D. Scheinman, Design of a computer controlled manipulator, MS Thesis, Stanford University, 1969.

[36] B. Shimano, B. Roth, On Force Sensing Information and Its Use in Controlling Manipulators, in: IFAC Proceedings Volumes, Tokyo, Japan, 1977: pp. 119–126. https://doi.org/10.1016/S1474-6670(17)66591-1.

[37] H. Van Brussel, H. Belien, H. Thielemans, Force sensing for advanced robot control, Robotics. 2 (1986) 139–148. https://doi.org/10.1016/0167-8493(86)90050-1.

[38] L.-P. Chao, K.-T. Chen, Shape optimal design and force sensitivity evaluation of six-axis force sensors, Sens. Actuator A Phys. 63 (1997) 105–112. https://doi.org/10.1016/S0924-4247(97)01534-3.

[39] D.V. Dao, T. Toriyama, J. Wells, S. Sugiyama, Six-degree of freedom micro force-moment sensor for application in geophysics, in: Technical Digest. MEMS 2002 IEEE International Conference. Fifteenth IEEE International Conference on Micro Electro Mechanical Systems (Cat. No.02CH37266), Las Vegas, Nevada, USA, 2002: pp. 312–315. https://doi.org/10.1109/MEMSYS.2002.984265.

[40] W. Shi, S.D. Hall, A novel six-axis force sensor for measuring the loading of the racing tyre on track, in: Proceedings of 1st International Conference on Sensing Technology (ICST2005), Palmerston North, New Zealand, 2005: pp. 408–413.

[41] J. Ma, A. Song, Fast Estimation of Strains for Cross-Beams Six-Axis Force/Torque Sensors by Mechanical Modeling, Sensors. 13 (2013) 6669–6686. https://doi.org/10.3390/s130506669.

[42] G.-S. Kim, Design of a six-axis wrist force/moment sensor using FEM and its fabrication for an intelligent robot, Sens. Actuator A Phys. 133 (2007) 27–34. https://doi.org/10.1016/j.sna.2006.03.038.

500 [43] G.-S. Kim, H.-J. Shin, J. Yoon, Development of 6-axis force/moment sensor for a humanoid
501 robot's intelligent foot, Sens. Actuator A Phys. 141 (2008) 276–281.
502 https://doi.org/10.1016/j.sna.2007.08.011.

503 [44] G. Mastinu, M. Gobbi, G. Previati, A New Six-axis Load Cell. Part I: Design, Exp. Mech. 51
504 (2011) 373–388. https://doi.org/10.1007/s11340-010-9355-1.

505 [45] M. Gobbi, G. Previati, P. Guarneri, G. Mastinu, A New Six-Axis Load Cell. Part II: Error
506 Analysis, Construction and Experimental Assessment of Performances, Exp. Mech. 51 (2011) 389–
507 399. https://doi.org/10.1007/s11340-010-9350-6.

508 [46] Y. Sun, Y. Liu, M. Jin, H. Liu, Design and optimization of a novel six-axis force/torque sensor
509 with good isotropy and high sensitivity, in: 2013 IEEE International Conference on Robotics and
510 Biomimetics (ROBIO), IEEE, Shenzen, China, 2013: pp. 631–638.
511 https://doi.org/10.1109/ROBIO.2013.6739530.

512 [47] A. Kazerooni, H. Akbari, Proposing an index for qualitative comparison of six-axis
513 force/torque sensors and optimization of Maltese cross geometry to reduce cross-coupling error,
514 Modares Mech. Eng. 17 (2017) 153–164.

515 [48] L. Schickl, K. Dorer, M. Wülker, U. Hochberg, Development of a Six-Axis Force and Torque
516 Sensor for the Humanoid Robot Sweaty 2.0, in: Proceedings of the 11th Workshop on Humanoid
517 Soccer Robots, 2016 IEEE-RAS International Conference on Humanoid Robots, Cancun, Mexico,
518 2016.

519 [49] D. Chen, A. Song, A. Li, Design and Calibration of a Six-axis Force/torque Sensor with Large
520 Measurement Range Used for the Space Manipulator, Procedia Eng. 99 (2015) 1164–1170.
521 https://doi.org/10.1016/j.proeng.2014.12.699.

[50] J. Huang, C.Y. Wong, D.T. Pham, Y. Wang, C. Ji, S. Su, W. Xu, Q. Liu, Z. Zhou, Design of a Novel Six-Axis Force/Torque Sensor based on Optical Fibre Sensing for Robotic Applications, in: Proceedings of the 15th International Conference on Informatics in Control, Automation and Robotics (ICINCO 2018), Porto, Portugal, 2018: pp. 517–524. https://doi.org/10.5220/0006911705170524.

[51] Y. Wang, G. Zuo, X. Chen, L. Liu, Strain Analysis of Six-Axis Force/Torque Sensors Based on Analytical Method, IEEE Sens. J. 17 (2017) 4394–4404. https://doi.org/10.1109/JSEN.2017.2703160.

[52] G.-S. Kim, D.-I. Kang, S.-H. Rhee, Design and fabrication of a six-component force/moment sensor, Sens. Actuator A Phys. 77 (1999) 209–220. https://doi.org/10.1016/S0924-4247(99)00208-3.

[53] C. Yuan, L.-P. Luo, Q. Yuan, J. Wu, R.J. Yan, H. Kim, K.-S. Shin, C.-S. Han, Development and evaluation of a compact 6-axis force/moment sensor with a serial structure for the humanoid robot foot, Measurement. 70 (2015) 110–122. https://doi.org/10.1016/j.measurement.2015.03.027.

[54] B. Wu, P. Cai, Decoupling Analysis of a Sliding Structure Six-axis Force/Torque Sensor, Meas. Sci. Rev. 13 (2013) 187–193. https://doi.org/10.2478/msr-2013-0028.

[55] R. Bekhti, Geometrical, mechanical and transduction techniques for designing multi-axis force-torque sensors for robotic applications, PhD Thesis, École de technologie supérieure, Université du Québec, 2015.

[56] Cunningham D.M., G.W. Brown, Two devices for measuring the forces acting on the human body during walking, Proc. Soc. Exp. Stress Anal. 9 (1952) 75–90.

[57] J.P. Paul, Forces at the human hip joint, PhD Thesis, University of Glasgow, 1967.

[58] M.A. Stroud, The behaviour of sand at low stress levels in simple shear apparatus, PhD Thesis, University of Cambridge, 1971.

[59] P.L. Bransby, Cambridge contact stress transducers, Department of Engineering, University of Cambridge, 1972.

[60] W. Huang, H. Jiang, H. Zhou, Mechanical analysis of a novel six-degree-of-freedom wrist force sensor, Sens. Actuator A Phys. 35 (1993) 203–208. https://doi.org/10.1016/0924-4247(93)80153-8.

[61] D. Stewart, A Platform with Six Degrees of Freedom, Proc. Inst. Mech. Eng. 180 (1965) 371–386. https://doi.org/10.1243/PIME_PROC_1965_180_029_02.

[62] C.-G. Kang, Closed-form force sensing of a 6-axis force transducer based on the Stewart platform, Sens. Actuator A Phys. 90 (2001) 31–37. https://doi.org/10.1016/S0924-4247(00)00564-1.

[63] A. Romiti, M. Sorli, Force and moment measurement on a robotic assembly hand, Sens. Actuator A Phys. 32 (1992) 531–538. https://doi.org/10.1016/0924-4247(92)80039-6.

[64] M. Sorli, N. Zhmud́, Investigation of force and moment measurement system for a robotic assembly hand, Sens. Actuator A Phys. 37–38 (1993) 651–657. https://doi.org/10.1016/0924-4247(93)80111-S.

[65] C. Ferraresi, S. Pastorelli, M. Sorli, N. Zhmud', State and dynamic behavior of a high stiffness stewart platform-based force/torque sensor, J. Robot. Syst. 12 (1995) 883–893. https://doi.org/10.1002/rob.4620121211.

[66] J.S. Dai, D.R. Kerr, A six-component contact force measurement device based on the Stewart platform, Proc. Inst. Mech. Eng. C. 214 (2000) 687–697. https://doi.org/10.1243/0954406001523696.

[67] T.A. Dwarakanath, B. Dasgupta, T.S. Mruthyunjaya, Design and development of a Stewart platform based force–torque sensor, Mechatronics. 11 (2001) 793–809. https://doi.org/10.1016/S0957-4158(00)00048-9.

566 [68] J. Zhenlin, G. Feng, Z. Xiaohui, Design and analysis of a novel isotropic six-component
567 force/torque sensor, Sens. Actuator A Phys. 109 (2003) 17–20. https://doi.org/10.1016/S0924-
568 4247(03)00299-1.

569 [69] R. Ranganath, P.S. Nair, T.S. Mruthyunjaya, A. Ghosal, A force–torque sensor based on a
570 Stewart Platform in a near-singular configuration, Mech. Mach. Theory. 39 (2004) 971–998.
571 https://doi.org/10.1016/j.mechmachtheory.2004.04.005.

572 [70] S. Bhavikatti, R. Ranganath, A. Ghosal, A near-singular, flexure jointed, moment sensitive
573 Stewart platform based force-torque sensor, in: Proceedings of the 13th National Conference on
574 Machines and Mechanisms, Bangalore, India, 2007: pp. 67–74.

575 [71] U. Seibold, B. Kubler, G. Hirzinger, Prototype of Instrument for Minimally Invasive Surgery
576 with 6-Axis Force Sensing Capability, in: Proceedings of the 2005 IEEE International Conference on
577 Robotics and Automation, IEEE, Barcelona, Spain, 2005: pp. 496–501.
578 https://doi.org/10.1109/ROBOT.2005.1570167.

579 [72] M. Luo, E. Shimizu, F. Zhang, M. Ito, Development of a Stewart Platform-based 6-axis Force
580 Sensor for Robot Fingers, in: ICCAS2005, Gyeonggi-do, South Korea, 2005.

581 [73] J. Yao, Y. Hou, L. Lu, Y. Zhao, Analysis of a Pre-stressed Six-component Force/Torque
582 Sensor Based on Stewart Platform, in: Proceedings of the 2006 IEEE International Conference on
583 Robotics and Biomimetics, IEEE, Kunming, China, 2006: pp. 346–350.
584 https://doi.org/10.1109/ROBIO.2006.340200.

585 [74] T.A. Dwarakanath, D. Venkatesh, Simply supported, 'Joint less' parallel mechanism based
586 force–torque sensor, Mechatronics. 16 (2006) 565–575.
587 https://doi.org/10.1016/j.mechatronics.2006.03.013.

588 [75] M.S. Müller, L. Hoffmann, T.C. Buck, A.W. Koch, Fiber Bragg Grating-Based Force-Torque
589 Sensor with Six Degrees of Freedom, Int. J. Optomechatronics. 3 (2009) 201–214.
590 https://doi.org/10.1080/15599610903144146.

591 [76] G.-S. Kim, H.-D. Lee, Development of a six-axis force/moment sensor and its control system
592 for an intelligent robot's gripper, Meas. Sci. Technol. 14 (2003) 1265–1274.
593 https://doi.org/10.1088/0957-0233/14/8/311.

594 [77] R. Haslinger, P. Leyendecker, U. Seibold, A Fiberoptic Force-Torque-Sensor for Minimally
595 Invasive Robotic Surgery, in: 2013 IEEE International Conference on Robotics and Automation,
596 IEEE, Karlsruhe, Germany, 2013: pp. 4390–4395. https://doi.org/10.1109/ICRA.2013.6631199.

597 [78] R. Richardson, M. Brown, B. Bhakta, M.C. Levesley, Design and control of a three degree of
598 freedom pneumatic physiotherapy robot, Robotica. 21 (2003) 589–604.

599 [79] J.H. Kim, D.I. Kang, H.H. Shin, Y.K. Park, Design and analysis of a column type multi-
600 component force/moment sensor, Measurement. 33 (2003) 213–219.

601

Table 1 Summary of three DOF cross-beam force sensors documented in the literature

Reference	3DOF type	Strain sensing (number of sensors)	Construction comments	Sensor size	Measurement range[a]	Measurement particulars[b]	Application[c]
Bekhti et al. [25]	A	Capacitance (4)	Plastic structure, pairs of parallel beams in cross	20 mm × 20 mm × 14 mm	$F_x = F_y = 60$ N, $F_z = 100$ N	R: 0.05%	Robot control
Fernandez Fernandez et al. [14]	C	FBG (8)	Rigid joints, square cross-section beams	Beam lengths = 50 mm, Beam cross section = 4 mm × 4 mm, Central platform radius = 25 mm	$F_z = 475$ N, $M_x = M_y = 6.5$ Nm	-	Robot control (in EM noisy environments)
Fontana et al. [24]	A	ERSG (16)	Rigid joints, vertically compliant beams	Beam lengths = 7.4 mm, Beam cross section = 3 mm × 0.4 mm	$F_x = F_y = F_z = \pm 5$ N	R: 0.04% CE: 0.1% NE: 0.06% HE: 0.21%	Dual-finger haptic interface
Kim et al. [27]	B	ERSG (40)	Laterally flexible plate beams in both cross-members and frame, both instrumented	Beam lengths = 17 mm, Beam cross section = 14 mm × 1.8 mm	$F_x = F_y = 100$ N, $M_z = 2$ Nm	CE: 0.01 – 1.7%	General sensor development
Lin et al. [33]	B	ERSG (16)	Eight-spoked design with rigid joints	Diameter = 290 mm, Thickness = 10 mm	$F_x = F_y = 14$ kN, $M_z = 3000$ Nm	HE: 0.9 – 1.1% NE: 0.6-0.9% RE: 0.5%	Wheel force measurement
Richardson et al. [78]	A	ERSG (8)	Rigid joints, vertically compliant beams	70 mm × 70 mm (overall). Beam cross sections = 5 mm × 2 mm	$F_x = F_y = F_z = \pm 20$ N	-	Control of pneumatic physiotherapy robot
Valdastri et al. [23]	A	Piezoresistive (4)	Silicon structure, piezoresistors obtained by ion implantation	2.3 mm × 2.3 mm × 1.3 mm	$F_x = F_y = 0$-0.4 N, $F_z = 0$-2.5 N	S: 0.0254 - 0.026 N^{-1} (F_x, F_y, F_z).	Interface force measurement for prosthetic

						NE: 0.28% (F_z) – 2.5% (F_x, F_y)	
Xiong et al. [26]	A	FBG (5)	Rigid joints, vertically compliant beams	Diameter = 72 mm, Thickness = 26 mm	$F_x = F_y = \pm 50$ N, F_z = 0-60 N	S*:* 11.259 - 23.366 pm/N, F_z = 11.259 pm/N RE: 2.23 – 2.45% CE: 1.28 – 4.05%	Robot plantar force measurement

[a]Measurement ranges as reported by the respective authors or deduced from calibration plots

[b]Measurement particulars as reported by the respective authors; R = resolution, S= sensitivity, NE = nonlinearity error, HE = hysteresis error, RE = repeatability error, CE = coupling error

[c]Studies that do not refer to a specific application for the development of the respective sensor are listed here as 'general sensor development'

Table 2 Summary of six DOF cross-beam force sensors documented in the literature

Reference	Strain sensing (number of sensors)	Construction comments	Sensor size	Measurement range[a]	Measurement particulars[b]	Application[c]
Chao and Chen [38]	ERSG (16, 24, 32, 48)	Ball-bearing frame-beam joints	-	$F_x = F_y = 392$ N, $F_z = 784$ N, $M_x = M_y = 20$ Nm, $M_z = 29$ Nm	-	Wrist force sensor for robotic arm control
Chao and Yin [3]	ERSG (32)	Rigid-jointed	-	$F_x = F_y = 600$ N, $F_z = -1200$ N, $M_x = M_y = 3600$ Nmm, $M_z = 5400$ Nmm	-	Measuring reaction loads on human feet during locomotion
Chen et al. [49]	ERSG (-)	Compliant edge beams	Diameter = 370 mm (overall), height = 146 mm (overall)	$F_x = F_y = 10000$ N, $F_z = 12000$ N, $M_x = M_y = 2000$ Nm, $M_z = 3000$ Nm	R: < 20 N (F_x, F_y, F_z), < 3 N (M_x, M_y, M_z) CE: 0.03 – 1.84%	Control of large robotic manipulator for space applications
Dao et al. [39]	SSGs (18)	n-type micro silicon cross-beam with piezoresistors formed on surface through impurity diffusion	Overall chip dimensions = 3000 μm × 3000 μm × 400 μm	$F_x = F_y = F_z = 50$ N, $M_x = M_y = M_z = 2 \times 10^{-4}$ mNμm	S: 0.11 – 1.15 mV/mN (F_x, F_y, F_z), 3.4×10^{-3} - 4.6×10^{-4} mV/mNμm (M_x, M_y, M_z) NE: 0.5 – 2.5%	Measuring forces acting on a particle at the bed of a turbulent channel flow
Feng et al. [34]	ERSG (32)	Eight-spoke design with rigid joints	-	$F_x = F_y = 120$ kN, $F_z = 60$ kN, $M_x = M_y = 30$ kNm, $M_z = 60$ kN m	S: 10.5 – 110 μ/kN (F_x, F_y, F_z), 1.15 -1.20 μ/kNm (M_x, M_y, M_z) NE: 0.6 - 1.0 % HE: 0.6 – 1.3% RE: 0.4 – 0.65%	Wheel force transducer for a heavy truck
Huang et al. [50]	FBG (16)	Square cross-section beams with compliant plates at frame-beam joints	-	-	-	Robotic applications in harsh industrial environments
Kang et al. [30];	ERSG (24)	Square cross-section beams with compliant plates at frame-beam joints	Diameter = 92 mm (overall), height = 37 mm (overall)	$F_x = F_y = \pm 400$ N, $F_z = \pm 800$ N, $M_x = M_y = M_z = \pm 40$ Nm	CE: 0 – 3.2%	General sensor development

Kazerooni and Akbari [47]						
Kim et al. [52]	ERSG (56)	Dual cross-beam (3DOF-B and 3DOF-C, created from plate beams) connected at the frame	-	$F_x = F_y = F_z = 100$ N, $M_x = M_y = 1$ Nm, $M_z = 2$ Nm	CE: 0.01 – 2.0%	General sensor development
Kim [42]	ERSG (24)	Laterally compliant parallel-plate-beams in the frame, square cross-section cross-beam members	Diameter = 100 mm (overall), height = 31 mm (overall)	$F_x = F_y = F_z = 200$ N, $M_x = M_y = 2.5$ Nm, $M_z = 5$ Nm	CE: 0.07 – 2.85%	Robot wrist force sensor
Kim et al. [43]	ERSG (24)	Parallel-plate-beams in both cross-beam members and frame	Overall dimensions = 80 mm × 80 mm × 19 mm	$F_x = F_y = 500$ N, $F_z = 1000$ N, $M_x = M_y = 18$ Nm, $M_z = 8$ Nm	CE: 0.02 – 2.46%	Humanoid intelligent robot's foot
Kim et al. [31]	Capacitance (16)	Plastic cross-beam, grooves cut into beams to allow capacitive sensing	Diameter = 67 mm (overall), height = 30 mm (overall)	$F_x = F_y = F_z = 10$ N, $M_x = M_y = M_z = 0.16$ Nm	R: 5% (F_x, F_y, F_z), 12.5% (M_x, M_y, M_z) NE: 4.7 – 12.1%	Robotics applications
Ma and Song [41]	ERSG (24)	Square cross-section beams, with compliant members at the frame-beam joint	Overall dimensions = 96 mm × 96 mm × 7.2 mm	$F_x = F_y = \pm 100$ N, $F_z = -100$ N, $M_x = M_y = \pm 10$ Nm, $M_z = 12$ Nm	-	Robotics applications
Mastinu et al. [44]; Gobbi et al. [45]	ERSG (12)	Three-spoke design with 'spherical sliding joints'	Overall dimensions = 150 mm × 175 mm × 100 mm	$F_x = F_y = 5$ kN, $F_z = 10$ kN, $M_x = M_y = M_z = 0.5$ kNm	CE: < 1.0% A: 0.6% (F_x, F_y, F_z), 0.3% (M_x, M_y, M_z)	Characterisation of vehicle suspension systems
Palli et al. [32]	Optoelectronic (-)	Loads applied to a reflective surface mounted on cross-beam frame	Beam length = 16.5 mm, beam cross section = 4.8 mm × 1.5 mm	$F_x = F_y = F_z = \pm 50$ N, $M_x = M_y = M_z = \pm 1$ Nm	-	Robotics applications
Scheinman [35]	SSG (16)	Compliant supports at frame-beam joints	Diameter = 5.3 cm (overall), height = 2.5 cm (overall)	$F_x = F_y = 106$ N, $F_z = 167$ N, $M_x = M_y = 162$ Ncm, $M_z = 300$ Ncm	A: 1%	Wrist force sensor in the 'Stanford Arm' robotic manipulator

Schickl et al. [48]	ERSG (16)	Flexible members at frame-beam joints	-	$F_x = F_y$ = 800 N, F_z = 2100 N, $M_x = M_y = M_z$ = 50 Nm	-	Humanoid robot feet force measurement
Shi and Hall [40]	ERSG (16)	Square cross-section beams, spherical plain bearings at frame-beam joints	-	F_x = -1000 – 500 N, F_y -500 – 1250 N, F_z = -750 – 1000 N, M_x = -150 – 50 Nm, M_y = -125 – 50 Nm	R: 0.21 μ/kg (F_x, F_y, F_z), 1.16 μ/kgm (M_x, M_y, M_z)	Wheel force sensor
Sun et al. [46]	ERSG (32)	Double-bending-beam structures in cross and frame members, both instrumented	Diameter = 224 mm (overall), height = 117 mm (overall)	$F_x = F_y = F_z = \pm$ 500 N, $M_x = M_y = M_z = \pm$ 100 Nm	CE: 1.24 – 6.47%	Robotics applications
Van Brussel et al. [37]	ERSG (-)	Thin flexures at rim	-	$F_x = F_y = F_z$ = 20 N, $M_x = M_y = M_z$ = 1 Nm	-	Robot control
Wu and Cai [54]	ERSG (32)	Dual cross-beam (3DOF-B and 3DOF-C with double-hole structures) sliding structure within cylindrical shell	Diameter = 52 mm (overall), height = 28 mm (overall)	$F_x = F_y = F_z$ = 0-20 N, $M_x = M_y = M_z$ = 0-800 Nmm	S: 4.2 – 5.4 mV/N (F_x, F_y, F_z), 4.8 – 5.3 mV/Nmm (M_x, M_y, M_z) CE: 0.01 – 0.89%	Measuring forces between surgical tools and soft tissue
Yuan et al. [53]	ERSG (16)	Dual cross-beam (3DOF-B and 3DOF-C) connected at centre platform	Diameter = 50 mm (overall), Height = 12 mm (overall)	$F_x = F_y$ = 400 N, F_z = 1000 N, $M_x = M_y$ = 20 Nm, M_z = 10 Nm	S: 8.9 – 15.9 μV/N (F_y, F_z), 813.6 – 2260 μV/Nm (M_x, M_z) NE: 0.2 – 0.62% HE: 0.26 – 0.73% CE: 2.23 – 3%	Human gait analysis; Humanoid robot foot

[a]Measurement ranges as reported by the respective authors or deduced from calibration plots

[b]Measurement particulars as reported by the respective authors; R = resolution, S= sensitivity, NE = nonlinearity error, HE = hysteresis error, RE = repeatability error, CE = coupling error, A = accuracy

[c]Studies that do not refer to a specific application for the development of the respective sensor are listed here as 'general sensor development'

Table 3 Summary of column-type force sensors documented in the literature

Reference	Strain sensing (number of sensors)	Construction comments	Sensor size	Measurement range[a]	Measurement resolution[b]	Application[c]
Berme et al. [1]	ERSG (-)	Tubular cylinder with end flanges, machined from solid bar	Cylinder inner diameter = 26 mm, wall thickness = 2.3 mm, length = 56 mm (overall)	$F_x = F_y = 100$ N, $F_z = 1500$ N, $M_x = 150$ Nm, $M_y = 100$ Nm, $M_z = 20$ Nm	-	Biomechanical analysis of human gait within a prosthesis
Byrne and Houlsby [2]	ERSG (32)	Thin-walled aluminium cylinder with end flanges	Cylinder diameter = 27.5 mm, wall thickness = 0.475 mm, cylinder length = 70 mm	-	-	Force measurement during shallow foundation loading experiment
Cunningham and Brown [56]	ERSG (12[c])	Tubular cylinder with end flanges, machined from solid bar	Cylinder inner diameter = 5/8 in, wall thickness = 1/32 in, cylinder length = 5 in	Composite sensor[d]	-	Force plate for measurement of forces between ground and foot during walking
Kim et al. [79]	ERSG (16)	Solid steel cylinder	Diameter = 28.1 mm, length = 56.2 mm	$F_x = F_y = 6.1$ kN, $F_z = 50$ kN, $M_x = M_y = 228.5$ Nm, $M_z = 174.1$ Nm	NE: 0.03 – 0.17% HE: 0.01 – 0.15% RE: 0.03 – 0.15%	General sensor development
Paul [57]	SSG (12[c])	Tubular cylinder, drawn cylinder welded to end flanges	Cylinder inner diameter = 5/8 in, wall thickness = 1/32 in, cylinder length = 5.25 in (overall)	Composite sensor[d]	-	Force plate for measurement of forces between ground and foot during walking
Van Brussel et al. [37]	ERSG (-)	Four flexural aluminium strips between rigid rings	Diameter = 170 mm (overall), length = 60 mm (overall)	$F_x = F_y = F_z = 200$ N, $M_x = M_y = 100$ Nm, $M_z = 20$ Nm	R: 0.1 – 0.2%	Robot control in deburring applications
van der Laag [15]	ERSG (32); FBG (46)	Large hollow steel cylinder with end flanges,	Cylinder outer diameter = 170 mm, length = 520 mm (overall)	$F_x = F_y = \pm 200$ kN, $F_z = \pm 1000$ kN, $M_z = \pm 100$ kNm	NE: < 0.4%	To assess performance of 6-axis fatigue test loading rig

				instrumentation on inside and outside surface

[a]Measurement ranges as reported by the respective authors or deduced from calibration plots

[b]Measurement particulars as reported by the respective authors; R = resolution, S= sensitivity, NE = nonlinearity error, HE = hysteresis error, RE = repeatability error, CE = coupling error, A = accuracy

[c]Studies that do not refer to a specific application for the development of the respective sensor are listed here as 'general sensor development'

[d]Columns used in 'composite sensor' comprising a plate supported by four columns

Table 4 Summary of Stewart platform force sensors documented in the literature

Reference	Strain sensing (number of sensors)	Construction comments	Sensor size	Measurement range[a]	Measurement resolution[b]	Application[c]
Bhavikatti et al. [70]	ERSG (24)	Near-singularity design, flexural joints, ring –shaped strain sensing elements in legs	Diameter = 80 mm (overall), height = 47 mm (overall)	$F_x = F_y = 50$ N, $F_z = 200$ N, $M_x = M_y = M_z = 10000$ Nmm	-	Robot wrist force sensor
Dai and Kerr [66]	ERSG (-)	Pretensioned wires for legs connected to strain gauged cantilevers on the base	Radius to leg mounts on base = 40 mm, Effective platform height = 49 mm	-	-	Contact force measurement for robot grasping
Dwarakanath et al. [67]	ERSG (-)	Ball and socket joints, circular leg structures	Base radius = 4.5 cm, height = 8.7 cm	-	A: < 2%	Robotics applications
Dwarakanath and Venkatesh [74]	ERSG (24)	'Joint-less' design with deadweight pre-load	Height = 57.92 mm	ERSG example: $F_x = \pm 73$ N, $F_y = \pm 63$ N, $F_z = \pm 125$ N, $M_x = \pm 3394$ Nmm, $M_y = \pm 2939$ Nmm, $M_z = \pm 4899$ Nmm	A: < 4.6%	General sensor development
Haslinger et al. [77]	FBG (7)	Steel capillary legs containing optical fibres with FBGs	Diameter = 6.4 mm (overall), length = 6.5 mm (overall)	$F_x = F_y = F_z = 20$ N, $M_x = M_y = 15$ Ncm, $M_z = 10$ Ncm	HE: 0.03 – 0.53 N (F_x, F_y, F_z), 0.05 - 0.086 Nmm (M_x, M_y, M_z) CE: 1.85 N (F_z), 6.57 Nmm (M_y) A: 94.9%	Minimally invasive robotic surgery
Kang [62]	LVDT (6)	Legs made from a core, two springs and an LVDT, with ball and socket joints	-	$F_x = \pm 78$ N, $F_y = \pm 80$ N, $F_z = -180$ - 185 N, $M_x = \pm 9.5$ Nm, $M_y = \pm 8.9$ Nm, $M_z = \pm 13$ Nm	NE: 0.83 – 1.58% A: 3.5 – 7.5%	General sensor development

Kim and Lee [76]	FBG (6)	Legs formed by pre-tensioned FBGs, with a central column supporting platform	Diameter = 50 mm (overall), Height = 60 mm (overall)	$F_x = F_y = F_z = 38.52$ N, $M_x = M_y = M_z = 963$ Nmm	-	Minimally invasive robotic surgery
Luo et al. [72]	ERSG (12)	Thin-walled pipe legs, coincident ball joints	-	-	NE: 5.2%	Robot fingers
Müller et al. [75]	FBG (6)	Polymer sensor, pre-tensioned FBGs with a central structure supporting the platform	Sensor volume < 10 mm × 10 mm × 10 mm	$F_x = F_y = 10$ N, $F_z = 20$ N, $M_x = 20$ Ncm, $M_y = 14$ Ncm, $M_z = 10$ Ncm	R: 100 mN (F_z)	Minimally invasive robotic surgery
Romiti and Sorli [63]; Sorli and Zhmud [64]; Ferraresi et al. [65]	Single axis force transducers	Single-axis force transducers in legs, ball joints	Diameter = 180 mm (overall), height = 115 mm (overall)	$F_x = F_y = \pm 87$ N, $F_z = \pm 256$ N, $M_x = M_y = \pm 60.8$ Nm, $M_z = 70$ Nm	A: 0.015 – 0.4%	Robotic assembly hand
Seibold et al. [71]	ERSG (-)	Flexural hinges	Base radius = 4.2 mm, Leg length = 3.9 mm	$F_x = F_y = F_z = 2$ N, $M_x = M_y = M_z = 80$ Nmm	*R:* 0.05 N (F_x , F_y), 0.25 N (F_z)	Minimally invasive robotic surgery
Yao et al. [73]	ERSG (-)	Mechanical joints, pre-stressed central member	Platform radius = 30 mm, Base radius = 24 mm, leg length = 33 mm	$F_x = F_y = F_z = 200$ N, $M_x = M_y = 1$ Nm, $M_z = 0.4$ Nm	A: 0.2 – 0.3% (F_x, F_y, F_z), 2 – 11.9% (M_x, M_y, M_z)	General sensor development
Zhenlin et al. [68]	ERSG (24)	Cube-shaped platform with legs arranged on three orthogonal sides, flexural joints	Diameter = 42 mm (overall), height = 21 mm (overall)	-	-	Robotics applications

[a]Measurement ranges as reported by the respective authors or deduced from calibration plots

[b]Measurement particulars as reported by the respective authors; R = resolution, S= sensitivity, NE = nonlinearity error, HE = hysteresis error, RE = repeatability error, CE = coupling error, A = accuracy

[c]Studies that do not refer to a specific application for the development of the respective sensor are listed here as 'general sensor development'

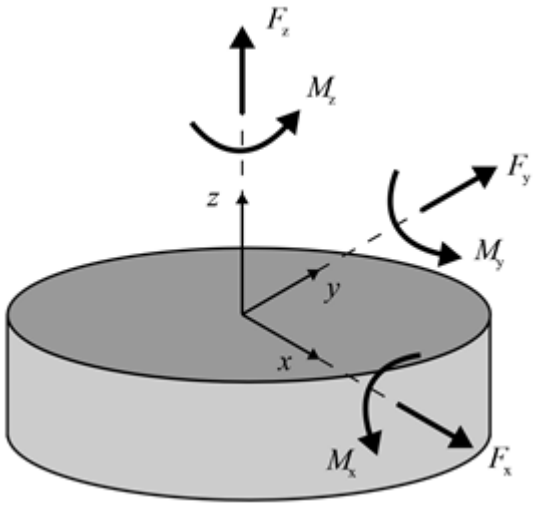

Figure 1 3D cartesian coordinate system adopted for force sensor analysis, showing the six general force and moment components

Figure 2 Illustration of the optical behaviour of a typical uniform FBG, showing indicative incident, reflected and transmitted light spectra

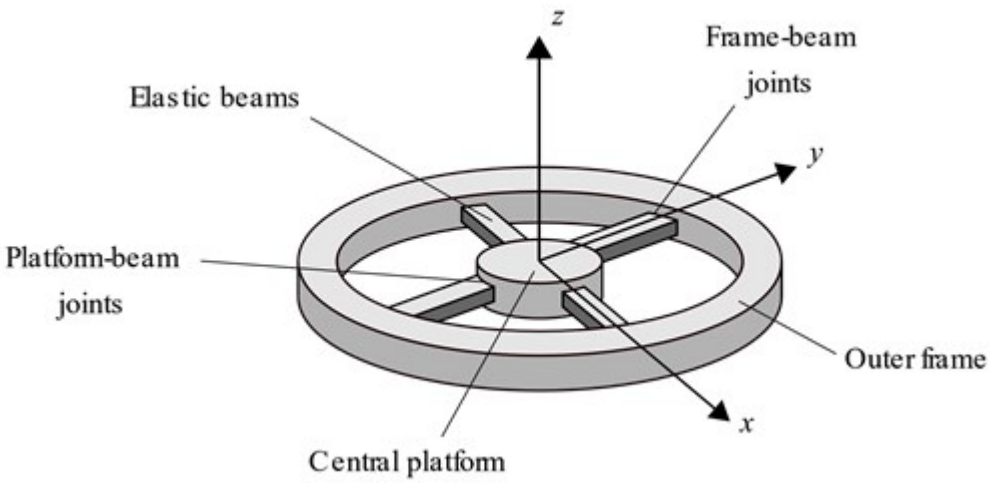

Figure 3 Illustration of a conventional cross-beam force sensor, showing the main elements of the structure

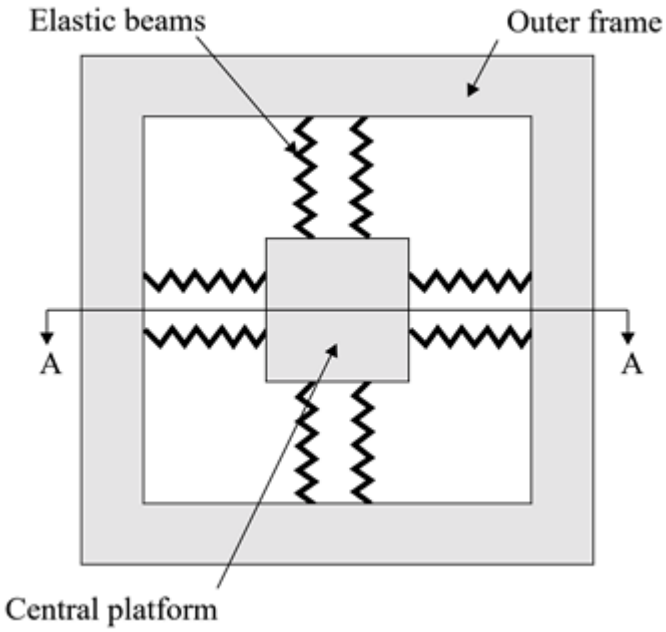

(a)

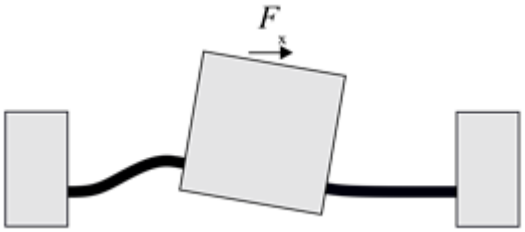

(b)

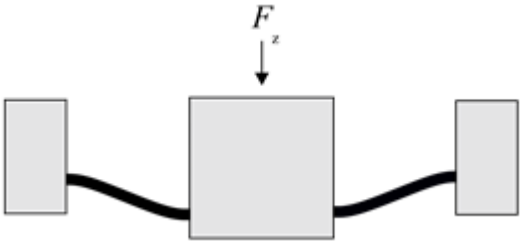

(c)

Figure 4 Schematic of a 3DOF-A cross-beam sensor proposed in [25]: (a) Plan view, (b) Secion A-A showing the exaggerated deformed shape under F_x loading and (c) Section A-A showing the exaggerated deformed shape under F_z loading

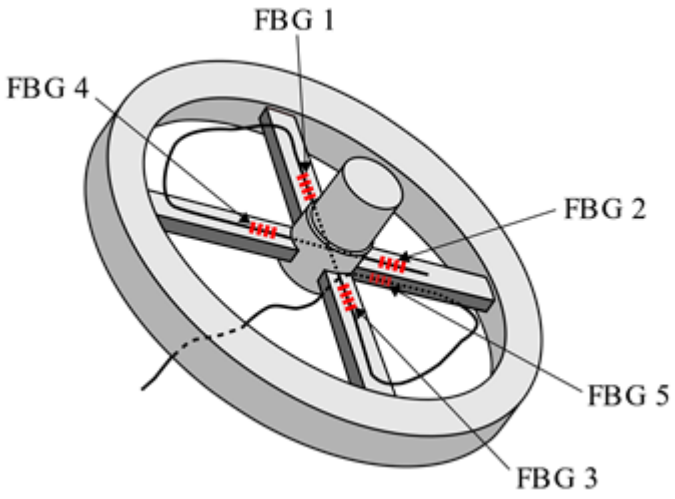

Figure 5 Schematic of a 3DOF-A cross-beam force sensor instrumented with five FBGs documented in [26]

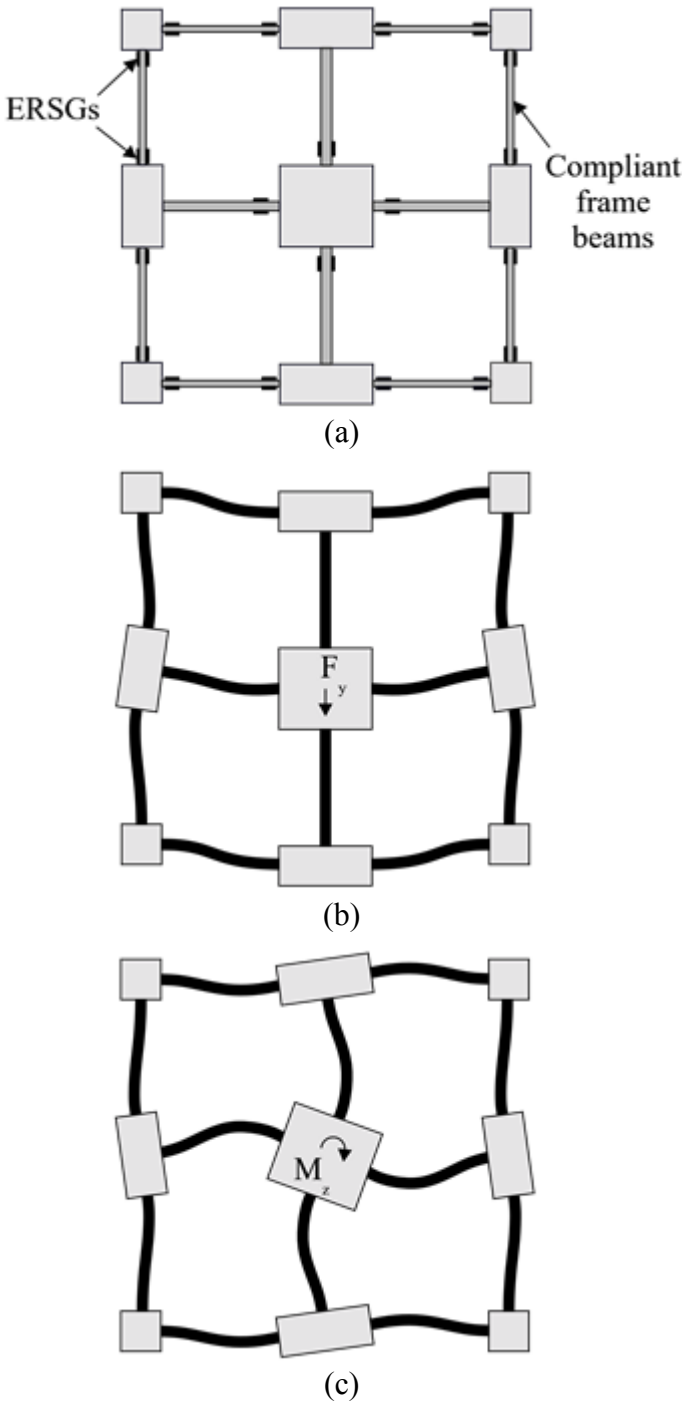

Figure 6 Three DOF cross-beam force sensor design proposed in [27] involving the use of highly - compliant elastic beam members: (a) structure showing locations of ERSGs, (b) exaggerated deformed shape of structure under F_y loading and (c) exaggerated deformed shape of structure under M_z loading

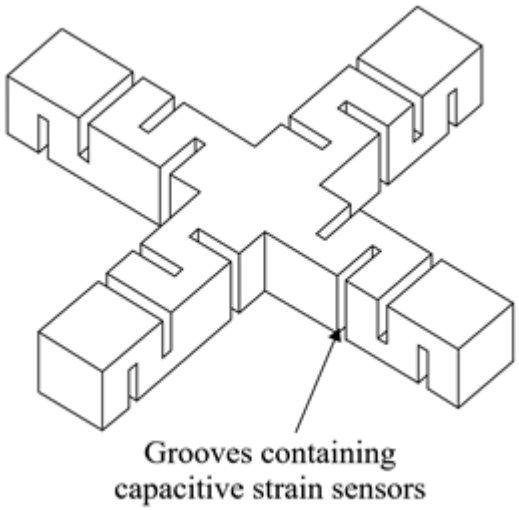

Figure 7 Six DOF cross-beam force sensor proposed in [31] showing grooves fabricated for capacitive strain-sensing

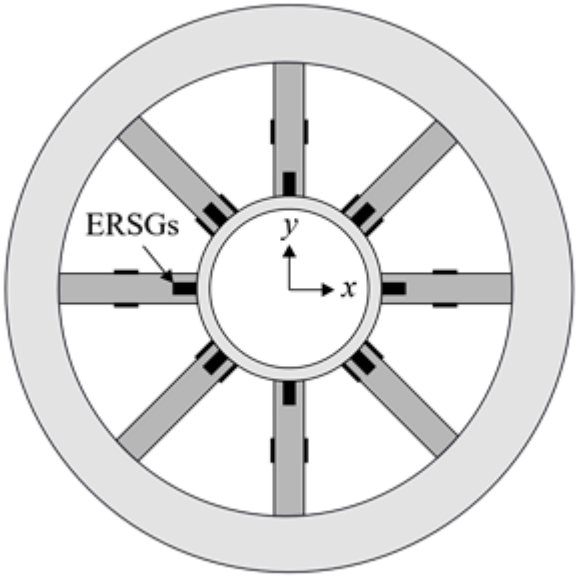

Figure 8 Schematic of a double-cross beam design for wheel force measurement proposed in [34] showing ERSG locations

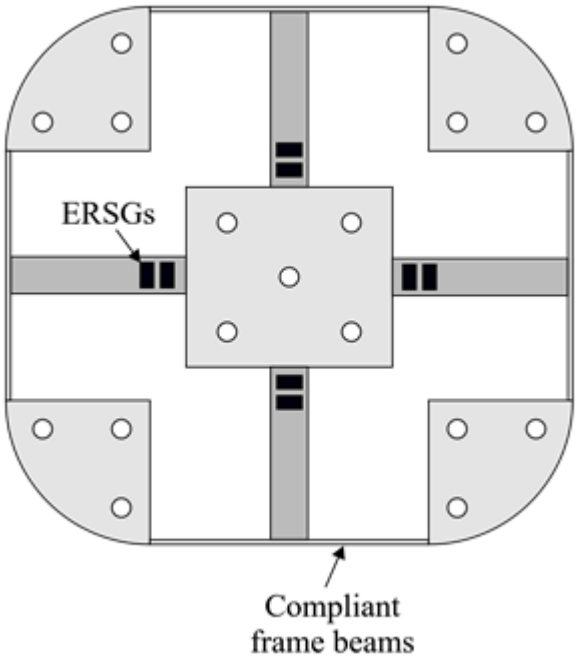

Figure 9 Illustration of a flexible-jointed six DOF cross-beam design documented in [37], showing highly-compliant plate elements in the outer frame and ERSG locations on the beam members

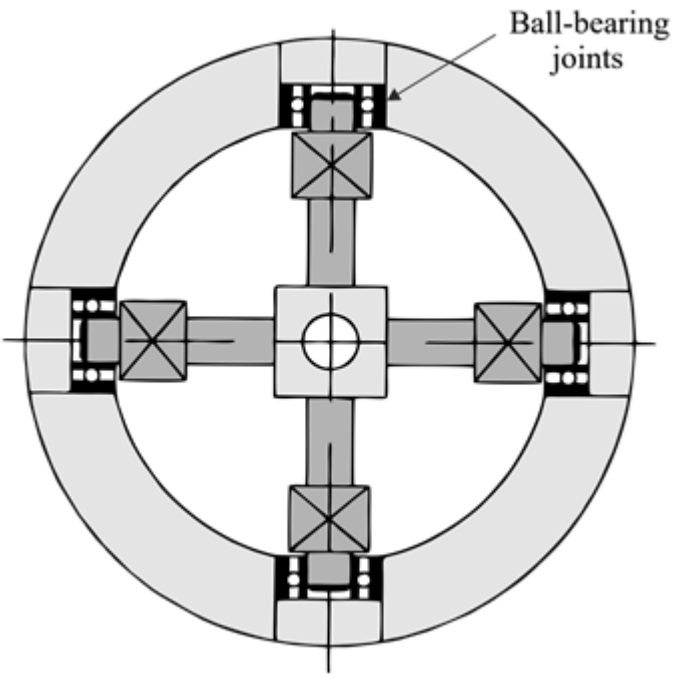

Figure 10 Six DOF cross-beam design proposed in [38] employing ball-bearings at the frame-beam joints

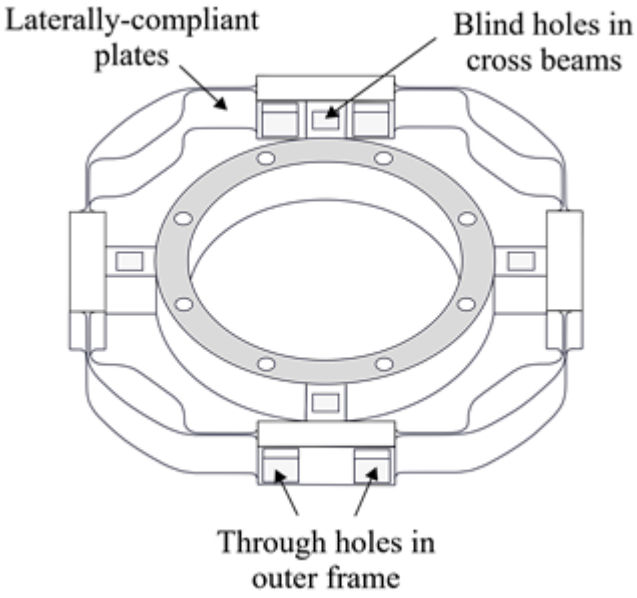

Figure 11 Three-dimensional view of the six DOF cross-beam sensor structure proposed in [46] involving laterally-compliant plates in the outer frame and blind holes and through holes in the beams and frame respectively to increase the load sensitivity

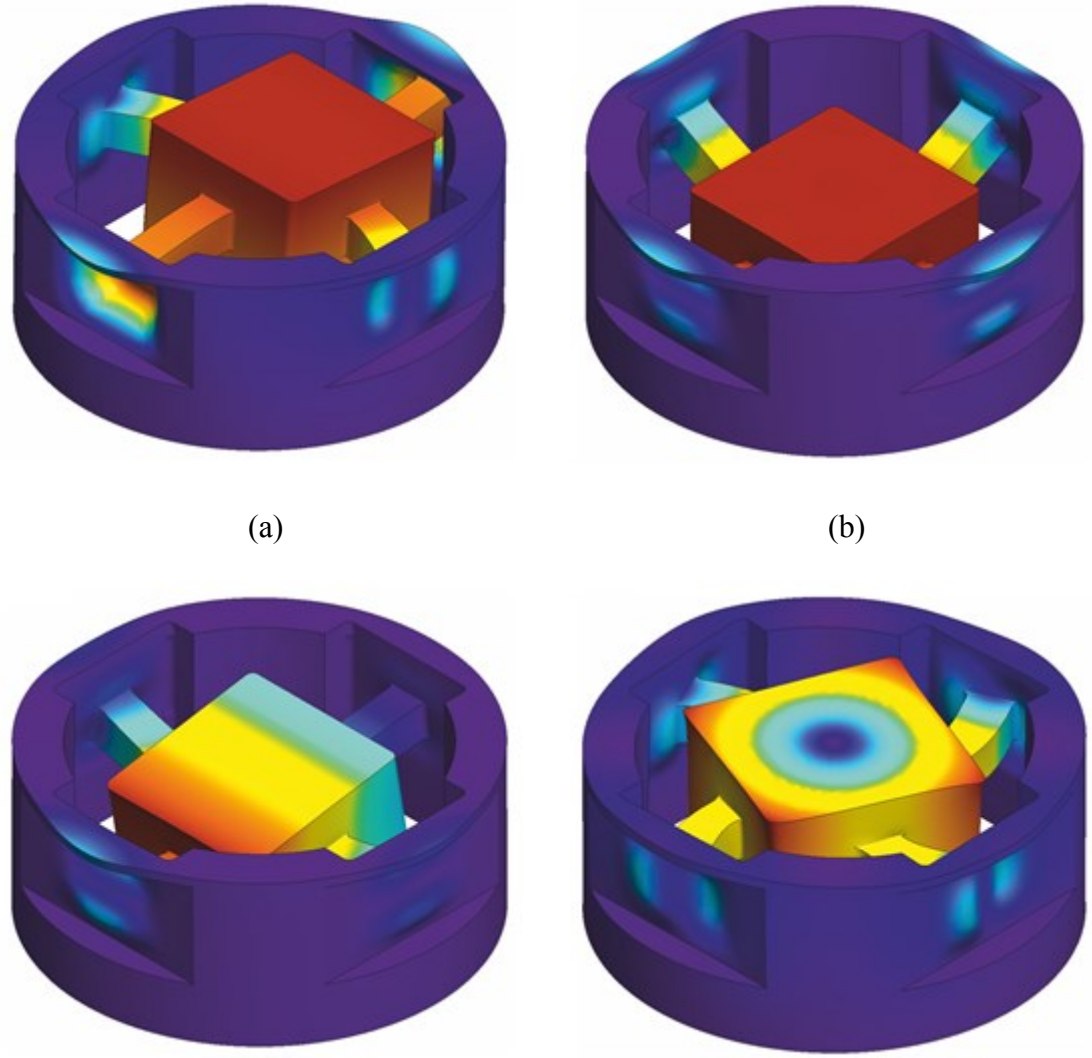

Figure 12 Illustration of the deformed shape of the flexible-jointed six DOF cross-beam sensor documented in [30] for (a) F_y, (b) F_z, (c) M_x, and (d) M_z loading. Contours denote resultant displacements

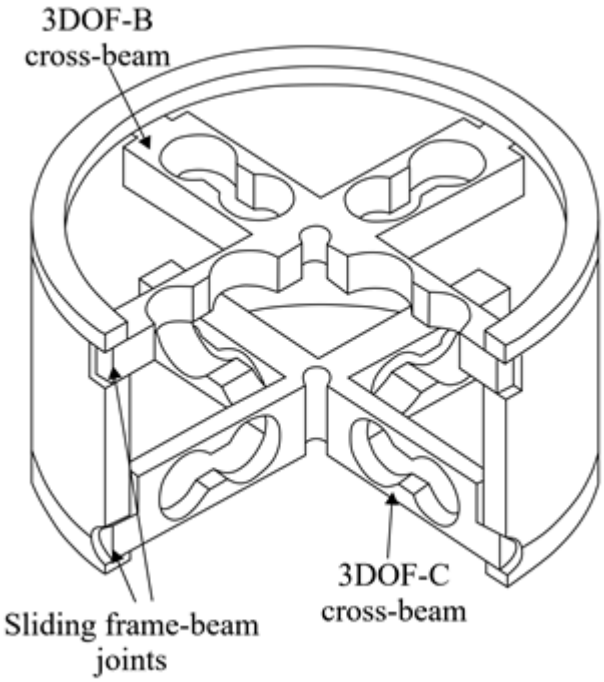

Figure 13 Dual-layer six DOF cross-beam force sensor proposed in [54] comprising an upper 3DOF-B cross-beam and a lower 3DOF-C cross-beam. The cross-beams are connected to the outer frame using sliding joints

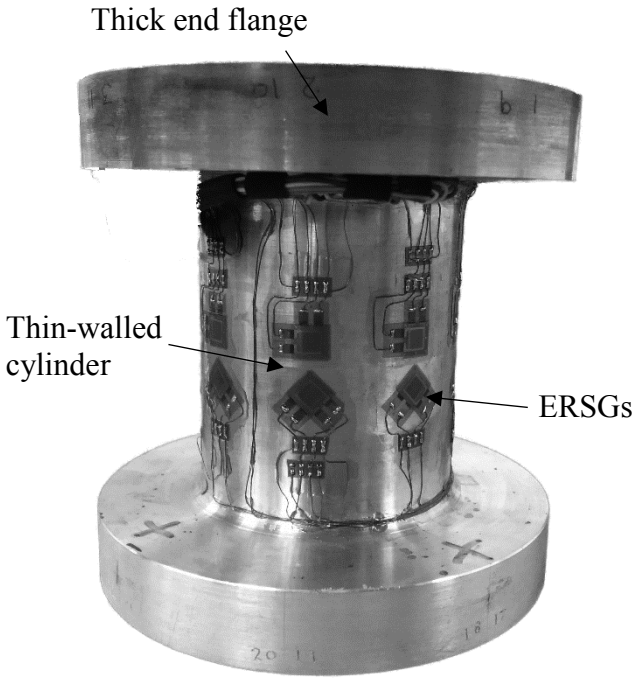

Figure 14 View of column-type load cell developed in [2] showing locations of ERSGs mounted on outer surface of the thin-walled cylinder sensor body

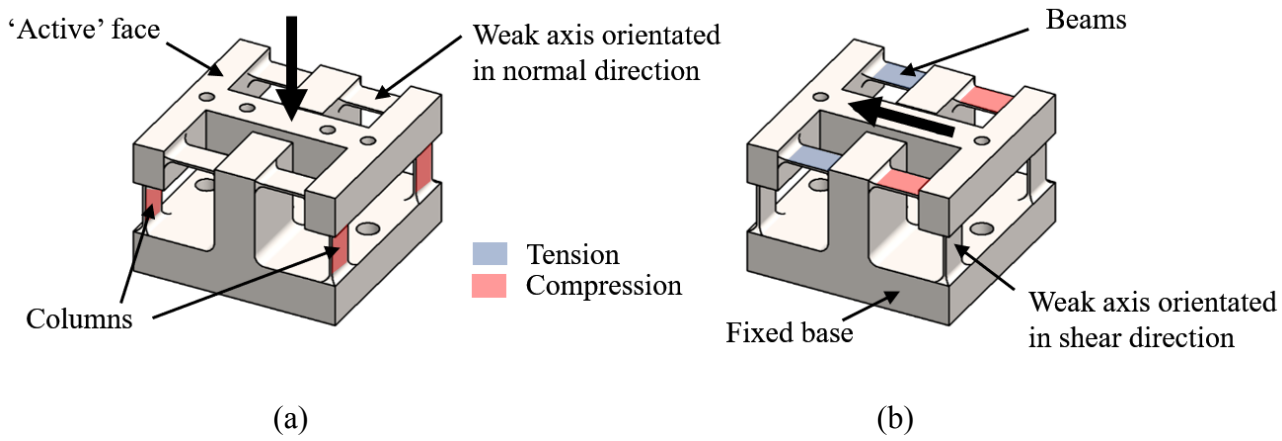

Figure 15 Beam-column force sensor proposed in [58] showing primary locations of tension and compression in the beams and columns under (a) F_z loading and (b) F_x loading

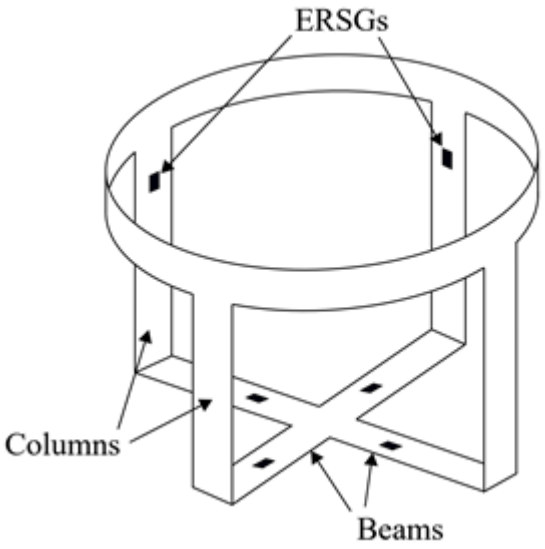

Figure 16 Schematic of the beam-column sensor design proposed in [60]

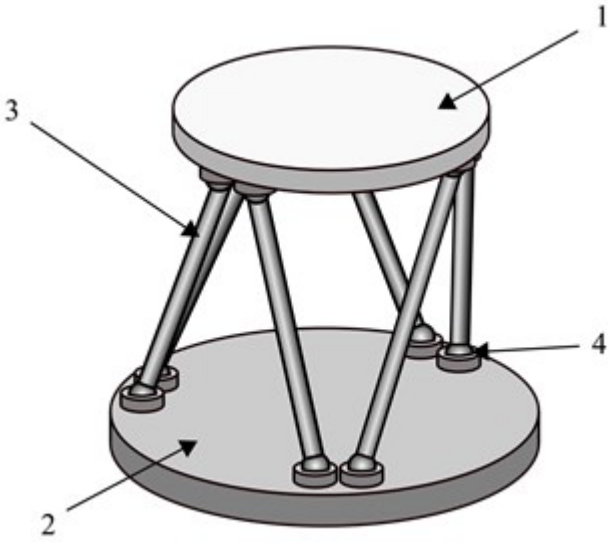

Figure 17 Illustration of a Stewart platform structure, showing the platform (1), fixed base (2), legs (3) and joints (4)

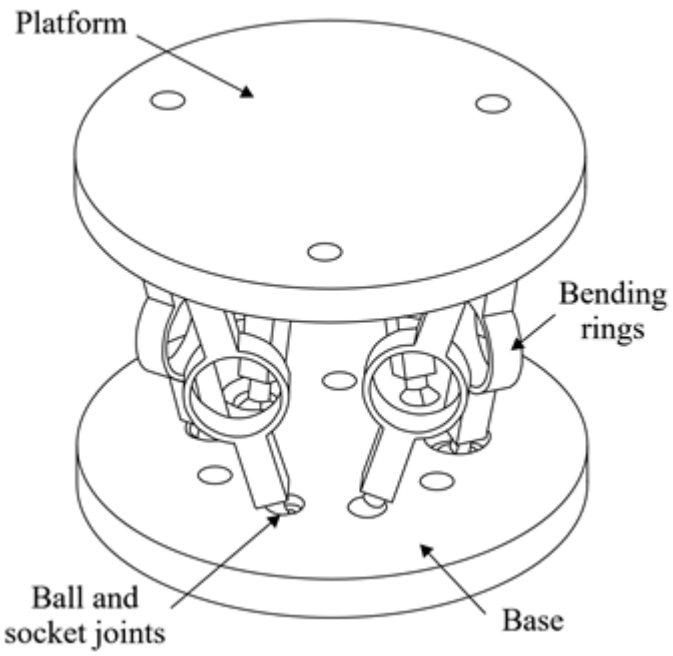

Figure 18 Stewart platform design proposed in [67] showing the strain gauged bending rings in the platform legs and the use of ball-and socket joints to connect the legs to the platform and base

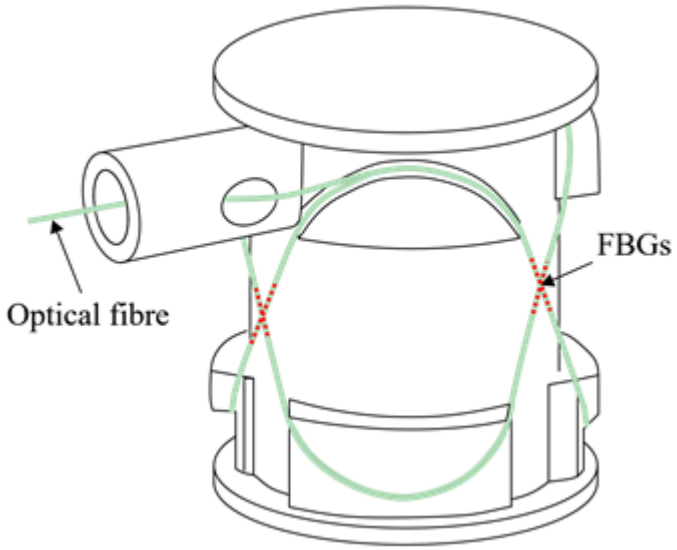

Figure 19 Stewart platform design using FBGs proposed in [75]